JOURNAL OF GEOPHYSICAL RESEARCH, VOL. 113, E02014, doi:10.1029/2007JE002991, 2008

Two aerodynamic roughness maps derived from Mars Orbiter Laser Altimeter (MOLA) data and their effects on boundary layer properties in a Mars general circulation model (GCM)

N. G. Heavens,[1] M. I. Richardson,[1] and A. D. Toigo[2]

Received 15 August 2007; revised 16 October 2007; accepted 4 December 2007; published 28 February 2008.

[1] Mechanical (forced convective) and free convective turbulent heat and momentum transfer in the lower atmosphere of a terrestrial planet has some dependence on the roughness characteristics of the surface, often quantified in terms of a single roughness parameter which is then used to calculate the coefficients that govern heat and momentum transport between the surface and the boundary layer. We take two different approaches for deriving this aerodynamic roughness parameter for Martian surfaces using data from the Mars Orbiter Laser Altimeter. We then use these two different roughness maps to force the boundary layer in a Mars general circulation model, primarily investigating differences in temperatures and the pressure cycle between the two simulations. While the pressure cycle does not vary significantly, spring and summer high-latitude temperatures are somewhat sensitive to the input roughness conditions. Daytime temperatures may vary up to 10 K seasonally, though zonally and annually averaged daytime temperatures vary only by $\sim$1 K. Our results can be explained by the dominance of mechanical over convective turbulent heat transfer processes on Mars. These simulations, however, use a prescribed atmospheric dust distribution and thus only provide a minimum estimate of the uncertainty in boundary layer temperatures because of this plausible range of aerodynamic roughness parameters. Since surface roughness determines the threshold wind velocity for dust lifting we anticipate a much larger effect of the aerodynamic roughness parameter on temperatures when the dust distribution is allowed to vary according to predicted lifting and transport.

Citation: Heavens, N. G., M. I. Richardson, and A. D. Toigo (2008), Two aerodynamic roughness maps derived from Mars Orbiter Laser Altimeter (MOLA) data and their effects on boundary layer properties in a Mars general circulation model (GCM), *J. Geophys. Res.*, *113*, E02014, doi:10.1029/2007JE002991.

1. Introduction

[2] An essential feature of a lower atmospheric model for a terrestrial planet is a parameterization to describe how heat and momentum are exchanged between the surface and the atmosphere. In a general circulation model (GCM) these exchange processes are often modeled using refinements of the boundary layer turbulence theory first described by *Obukhov* [1946]. One familiar result of this theory is the logarithmic increase of wind speed with height in a neutrally stratified layer from a level of no motion near the surface. The height of this level of no motion is alternately called ''the roughness parameter'' or ''the aerodynamic roughness height/length'' but is typically denoted z_0. The aerodynamic roughness height is usually treated as a spatially varying intrinsic property of the surface, corresponding to the effects of surface roughness elements such as rocks and trees on the atmospheric flow.

[3] An accurate map of z_0 is extremely useful for certain types of GCM simulations because many boundary layer processes within a GCM are highly sensitive to it, e.g., turbulent eddy diffusion of heat and momentum. Under convectively stable conditions, high z_0 will lead to vigorous and efficient mechanical mixing of heat and momentum and vice versa. However, in unstable conditions, low z_0 may result in enhanced vertical heat and momentum mixing because of convective processes. Thus boundary layer atmospheric temperatures may be nonlinearly sensitive to z_0. Of interest for both the Earth and Mars is the effect of z_0 on the transfer of momentum from the wind to sand and dust-sized particles on the surface. Smoother areas are more resistant to erosion and are less likely to be sites of initiation for dust-lifting activity such as dust storms.

[4] Strictly speaking, the aerodynamic roughness parameters for heat transport ($z_{0,h}$), momentum transport ($z_{0,m}$), and any other scalar transport are distinct. However, for the purposes of this study we will assume that these distinct aerodynamic roughness parameters are identical to $z_{0,m}$. The reasons for this choice are threefold. First, the only data

[1]Division of the Geological and Planetary Sciences, California Institute of Technology, Pasadena, California, USA.
[2]Center for Radiophysics and Space Research, Cornell University, Ithaca, New York, USA.

0148-0227/08/2007JE002991$09.00

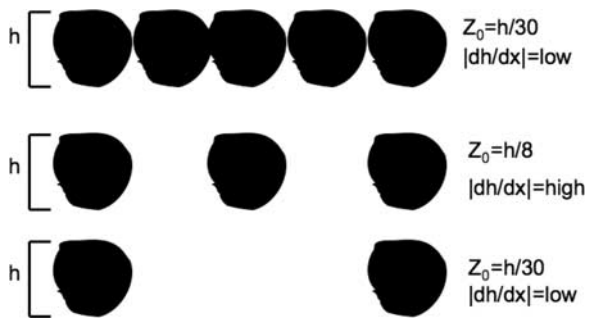

Figure 1. Cartoon of nonlinear dependence of z_0 on roughness element spacing and roughness element height, h, based on the results of wind tunnel experiments [after *Greeley and Iversen*, 1985, Figure 2.6]. The blobs represent semirounded sand particles. When the sand particles are closely packed as in the top case, the measured z_0 is ~1/30 the diameter of the sand particle. When they are more widely spaced (~1 diameter spacing between the ends), the measured z_0 is ~1/8 the diameter of the sand particle. When they are even more widely spaced, the measured z_0 is ~1/30 of the diameter of the sand particle.

available for calibrating z_0 on Mars is a measurement of the aerodynamic roughness parameter for momentum [*Sullivan et al.*, 2000]. Second, a future research goal will be to understand the sensitivity of dust transport processes to z_0, so the roughness parameter for momentum is of chief importance. Third, we will use a GCM that is only capable of using one type of aerodynamic roughness parameter at present. *Chen et al.* [1997] provide a good discussion of the problems with using a single type of z_0 and an example of how a boundary layer scheme may be modified to account for the different length scales of heat and momentum transport, but the implementation of such a scheme for Mars awaits appropriate observational data.

[5] Remote sensing provides a variety of avenues for investigating the roughness characteristics of Mars such as radar, laser sounding, and mapping of roughness elements in visual and infrared imagery. However, the transfer function between the physical roughness characteristics that interest geologists and z_0 is not always straightforward.

[6] In this study, we first describe two ways of conceptualizing an important nonlinearity in the transfer function (section 2). Next, we construct two different maps of aerodynamic roughness length based on Mars Orbiter Laser Altimeter (MOLA) data: one based on topography and the other based on the scattering of the MOLA beam by the surface (section 3). Finally, we use each roughness map to force a Mars GCM, the Mars implementation of the Planetary Weather Research and Forecasting Model (MarsWRF) [*Richardson et al.*, 2007], and examine differences in their output boundary layer temperatures (section 4). We then summarize our results (section 5).

2. Effects of Roughness Element Spacing on z_0

[7] In wind tunnel experiments, z_0 is typically a fraction of the height of the roughness elements. Moreover, the magnitude of this fraction is variable, ranging from 1/4 to 1/1200 [*Dong et al.*, 2002]. Some of this nonlinearity is due to the fact that z_0 is not really an intrinsic characteristic of the surface but also depends on the turbulence of the flow. Additional nonlinearity results from the distribution of roughness elements as mentioned by *Greeley and Iversen* [1985] (Figure 1).

[8] Note that this highly idealized one-dimensional approach to the effect of roughness element distribution on z_0 suggests the relation $z_0 \propto |dh/dx|$. Actual roughness element distributions, however, typically are two dimensional. Consider an area with a number of sites, N_s. Some number of these sites, N_0, are occupied by a roughness element of height, h. We make no assumption about how uniformly distributed the roughness elements are, but it is helpful to pretend that all the roughness elements are not clumped all to one side. We then define F as the fractional occupation of sites, N_o/N_s, and so the mean elevation of the area relative to its original surface height becomes hF. Then the population variance of the topography in the area (σ_h^2) is

$$\begin{aligned}\sigma_h^2 &= \frac{1}{N_s}\left[(N_s - N_o)(0 - hF)^2 + N_o(h - hF)^2\right] \\ &= \left[(1-F)\left(h^2F^2\right) + Fh^2(1-F)^2\right] \\ &= Fh^2 - h^2F^2. \end{aligned} \quad (1)$$

[9] Thus $\sigma_h^2 = h^2(F - F^2)$, and the standard deviation $\sigma_h = h(F - F^2)^{1/2}$ (Figure 2). Wind tunnel experiments show that $z_0(F)$ typically has a form very similar to σ_h or σ_h^2 [*Dong et al.*, 2002]. However, some right skewing of the maximum from $F = 0.5$ is observed in *Dong et al.*'s [2002] data because the wind tunnel experiment scaling differs somewhat from the idealization above, which changes the definition of F in the wind tunnel experiment relative to its definition in the thought experiment. *Dong et al.* [2002], however, do fit their data with a function of the approximate form $A + BF + CF^{1.5} + DF^2$, where A, B, C, and D are functions of the free stream velocity, which is cosmetically similar to the statistical predictions. Note that the free

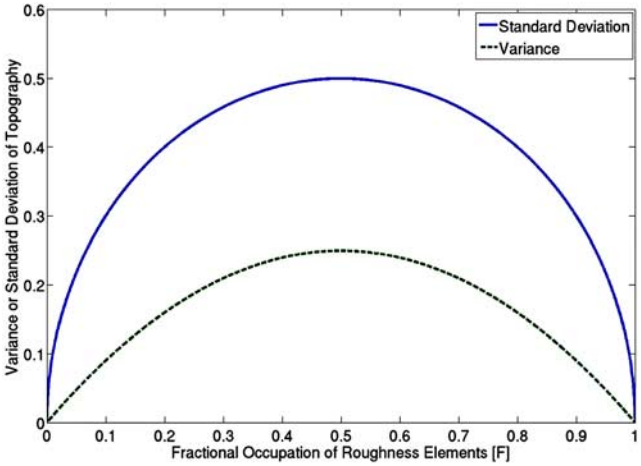

Figure 2. Thought experiment predictions of the dependence of the standard deviation and variance of topography on the fractional occupation of topographic features/roughness elements. Height (h) is fixed at 1.

stream velocity is the input wind velocity to the tunnel, corresponding to the velocity of the wind in the absence of frictional effects. Thus the statistical properties of physical roughness may have a relatively simple relation to z_0 such as $z_0 = k\sigma_h^n$, where k is a constant of proportionality and $1 < n < 2$. It would be, however, somewhat difficult to infer the relation between h and z_0 without access to *Dong et al.*'s [2002] original data, though it is clear that it is somewhat nonlinear, especially at high free stream velocity.

3. Deriving Maps of z_0 for Mars

[10] At present, the two most common approaches to determining relative z_0, that is, before calibration, of a planetary surface are (1) using the scattering behavior of an incident beam of radiation to infer relative roughness [e.g., *Marticorena et al.*, 2006] and (2) mapping and quantifying the density of more or less erodible roughness elements to infer relative roughness [e.g., *Sullivan*, 2002; *Hébrard et al.*, 2007]. The work of *Menenti and Ritchie* [1992] might fall into the second category, although they use high-resolution laser altimetry rather than visual observations in order to determine roughness element properties. If $z_0 \propto \sigma_h^n$ (see section 2), it might be possible to use statistical analysis of altimetry data in order to infer relative roughness. In this section we first describe the derivation of an aerodynamic roughness map from altimetry data that is scalable to a roughness scale of interest for an atmospheric application such as those used in boundary layer routines based on Smagorinsky deformation. Next, we describe the derivation of an aerodynamic roughness map from the scattering of the altimeter beam, which presumably provides a measure of relative roughness on the scale of the beam. Our goal is not to produce accurate aerodynamic roughness maps for Mars since the calibration data necessary to produce such a map is exceptionally limited (the Mars Pathfinder site only). Instead, we seek to produce two maps that will span a plausible range of z_0 for Mars.

3.1. Topographically Derived Aerodynamic Roughness Map for Mars

[11] *Kreslavsky and Head* [2000] (see also http://www.planetary.brown.edu/planetary/rough/, 2004) have published maps at $0.125° \times 0.125°$ resolution (2880×1440 cells) of topographic roughness derived from MOLA measurements. From the set of MOLA measurements in each cell, Kreslavsky and Head calculated a quantity they call c (the curvature), which is equal to $(h_{i+1} + h_{i-1} - 2h_i)/4L^2$, where h is the altitude relative to the MOLA datum and i, $i + 1$, and $i - 1$ represent the center and ends of a baseline, L, that separates individual MOLA measurements. Thus each cell will have multiple values of c in proportion to the number of MOLA measurements in the cell and the length of L. Kreslavsky and Head therefore map a parameter called C, which is the interquartile width of the distribution of c in each cell. Kreslavsky and Head's publicly available maps show roughness at $L = 0.6$, 2.4, and 9.2 km. Note that the definition of C implies a relation between C and σ_h. Also, since in the previous part we have argued for a relation between σ_h and z_0, we should be able to derive a relation to connect z_0 and C.

[12] We then assume that roughness at meter to kilometer scales follows fractal self-affine statistics such that $\sigma_h^2 = \alpha L^{2H}$, where α is a parameter of proportionality corresponding to the topographic variance in the special case of scale invariance ($H = 0$) and H is the Hurst exponent (also called the Hausdorff measure), which has a well-known range of (0, 1) for natural surfaces and describes how quickly the roughness properties of a surface change with scale [*Turcotte*, 1992; *Shepard and Campbell*, 1998]. If we assume that c within a given cell follows a normal distribution, we then can use the fact that the interquartile width $C \approx 1.38$ times the standard deviation:

$$C \approx 1.38\left[\sum_{j=1}^{N}(c-\bar{c})^2\right]^{1/2} \tag{2}$$

and derive an expression for C:

$$C = \frac{1.38}{4L^2}\left[\left(\sigma_{i+1}^2 + 2\sigma_{i+1}\sigma_{i-1}r_{i+1,i-1} - 4\sigma_{i+1}\sigma_i r_{i+1,i} - 4\sigma_{i-1}\sigma_i r_{i-1,i} + \sigma_{i-1}^2 + 4\sigma_i^2\right)\right]^{1/2}, \tag{3}$$

where σ_i^2 = variance of h_i and $r_{i,i-1}$ = correlation between h_i and h_{i-1}. C is maximized when the heights of the ends of the baseline are correlated and the heights of the ends anticorrelate with the height of the baseline center. C is minimized when the heights of the baseline ends and the center all correlate perfectly, i.e., flat terrain. Provided that σ_h is invariant within the cell, $C_{\max} = (1.38/4L^2)(4\sigma_h)$ and $C_{\min} = 0$, implying that $\bar{C} = (1.38/4L^2)(2\sigma_h)$, where $\bar{C}$ is the average value of C. We thus expect that $\sigma_h^2 \propto C^2L^4$. However, when we rearrange $C^2L^4 = \alpha L^{2H}$ in a form suitable for linear regression, $\ln C = 0.5 \ln \alpha + (H - 2) \ln L$, and fit each point on *Kreslavsky and Head*'s [2000] (see also http://www.planetary.brown.edu/planetary/rough/, 2004) roughness maps, we generally obtain values of H in the range (0, 2). Indeed, about half of the inferred H values are between 1 and 2. Since the range of H for real terrestrial surfaces and synthetically generated topography is (0, 1) [*Turcotte*, 1992] we are forced to conclude that $\sigma_h^2 \propto CL^2$, not C^2L^4.

[13] It is likely that the failure of our theory stems from improper treatment of c as a metric linear in h. However, c, the curvature, is the second derivative of h with respect to distance (approximated using the baseline L). Suppose that h is normally distributed with a probability distribution function:

$$\frac{1}{\sigma_h\sqrt{2\pi}}\exp\left(\frac{-h^2}{2\sigma_h^2}\right) = f(h). \tag{4}$$

The nth moment μ_n is then defined as [*Papoulis*, 1991]

$$\mu_n = \int_{-\infty}^{\infty} h^n f(h)dh. \tag{5}$$

If we differentiate $f(h)$ twice, we obtain

$$f''(h) = f(h)\left(\frac{h^2}{\sigma_h^4} - \frac{1}{\sigma_h^2}\right), \tag{6}$$

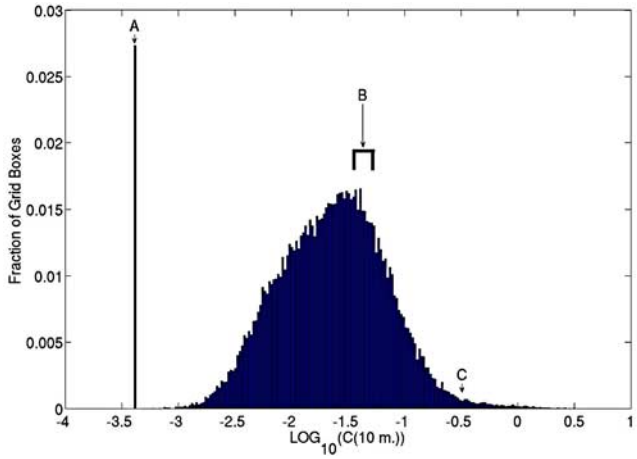

Figure 3. Histogram of $\log_{10} C$(10 m), based on randomly extracted C at 50,000 grid boxes. Outlier values associated with missing polar data are marked as A. The range of C(10 m) in the vicinity of the Mars Pathfinder site is marked as B. The beginning of the asymmetrically long tail in the distribution is marked as C. About 1% of grid boxes have $\log_{10} C(10\text{ m}) > -0.5$.

and if we apply the definition of the moment (5), the second moment of $f''(h)$ is the difference between the standardized fourth moment (μ_4/σ_h^4) (a form of the kurtosis) and the standardized second moment (μ_2/σ_h^2). The square root of this quantity should be proportionate to C. For a normal distribution, $\mu_n \propto \sigma_h^n$ [*Papoulis*, 1991]. Thus, for a distribution that is approximately, but not exactly, normal, it is possible that $((\mu_4/\sigma_h^4) - (\mu_2/\sigma_h^2))^{1/2} \propto \sigma_h^2$, implying $\sigma_h^2 \propto C$ and thus $\sigma_h^2 \propto CL^2$. However, a rigorous demonstration of this argument would require analysis of the curvature data directly. At that level of analysis it would be more efficient to derive σ_h^2 as a function of L from the altimetry data directly, and we recommend that this route to σ_h^2 be used in the future.

[14] Using the parameters α and H for each point (assuming $\sigma_h^2 \propto CL^2$), we then extrapolate C to a baseline of 0.01 km (10 m). This baseline corresponds to the approximate diameter of a median Martian dust devil [*Greeley et al.*, 2006] and thus a common scale of interactions between roughness elements and near-surface atmospheric flows. Excluding values associated with missing data at the poles and a potentially spurious long tail at $\log_{10} C(10\text{ m}) > -0.5$, the distribution of C(10 m) spans ~2.5 orders of magnitude (Figure 3). *Sullivan et al.* [2000] mention past estimates of z_0 on Mars from ~1 mm to 1 cm, though they measure z_0 of 3 cm at the Pathfinder site (certainly not the roughest part of Mars). Moreover, *Sullivan et al.* [2005] use $z_0 = 10^{-4}$ m to model aeolian processes at Meridiani Planum, though this choice appears arbitrary. It is fair to say that given the limited data set of z_0 measurements for Mars, the range of z_0 for Mars cannot be constrained. Terrestrial values in poorly vegetated terrain range from ~50 μm to > 15 cm (>3.5 orders of magnitude) [*Greeley et al.*, 1997; *Prigent et al.*, 2005]. Therefore, if z_0 is proportional to σ_h (same as proportionality to $C^{1/2}$), we may obtain an overly narrow range for Martian roughness (1.25 orders of magnitude). However, the data of *Dong et al.* [2002] do not appear to justify $z_0 \propto \sigma_h^n$, $n > 2$. Thus we assume that z_0 is proportionate to σ_h^2 and thus to C. For the sake of plausibility we allow a narrower range for z_0 in making the second map. We then calibrate C(10 m) to obtain z_0 by using the inference from Pathfinder wind measurements that z_0 at the Pathfinder site is ~3 cm [*Sullivan et al.*, 2000] and that $\log_{10} C$(10 m) at the Pathfinder site is ~−1.2. The value of z_0 measured by Pathfinder is thought to be an unusually high value for plains units [*Sullivan et al.*, 2000]. An interpolation of this data to a 36 × 64 (5° × 5.625°) grid is shown in Figure 4a.

3.2. MOLA Pulse Width–Derived Aerodynamic Roughness Map for Mars

[15] We obtained RMS total vertical roughness maps for Mars at 0.25° × 0.25° resolution from J. Garvin (unpublished data, 2002). Total vertical roughness is inferred from slope-corrected MOLA optical pulse width returns as described by *Garvin et al.* [1999]. The approximate baseline of these measurements is 75 m [*Neumann et al.*, 2003], implying that scattering will be preferential on this particular scale. We chose 16.62 cm to be the maximum z_0 to provide some basis for comparison with the Geophysical Fluid Dynamics Laboratory Mars GCM, which has a uniform z_0 of 16.62 cm [*Wilson and Hamilton*, 1996]. This value corresponds to an RMS roughness of 11 m. Note that the range of z_0 is roughly an order of magnitude (~1–10 cm) with typical values ~2 cm z_0 in the vicinity of the Mars Pathfinder site ranges from ~1.6 to 3.8 cm in this map. An interpolation of the pulse width z_0 to a 36 × 64 (5° × 5.625°) grid is shown in Figure 4b.

3.3. Differences Between Roughness Maps

[16] There are definite similarities between the two maps of z_0, such as the high z_0 associated with the lava flows surrounding Olympus Mons, the Tharsis Montes, and Aeolis Mensae. Moreover, both maps generally show smoother terrains in the high latitudes of both the northern and southern hemispheres. One difference between the two maps is the ranges of z_0 they show, which are due to different assumptions about the relation between z_0 and some measure of σ_h. The topographically derived map assumes $z_0 \propto \sigma_h^2$, while the pulse width map assumes $z_0 \propto \sigma_h$. Thus the topographically derived map accentuates broad roughness features such as in the vicinity of Hesperia Planum and Terra Tyrrhena (15°–25°S, 90°–110°E). Yet even if the topographically derived map assumed $z_0 \propto \sigma_h$, these two maps would differ somewhat and not just by a scale factor. Note, for instance, the strong differences between the maps at the south pole, Syrtis Major (10°S–20°N, 60°–80°E), and in Syria Planum and the surrounding regions (20°–0°S, 110°–80°W). Together these maps represent a plausible range of z_0 for Mars under typical conditions, not merely two differently stretched versions of the same data.

4. Effects of Different Roughness Maps in a Mars GCM

4.1. Methods

[17] We ran two MarsWRF simulations that differ only in the roughness maps used to define z_0, which were defined in section 3. The particular settings of the model used are those generally used for global runs as described by *Richardson et*

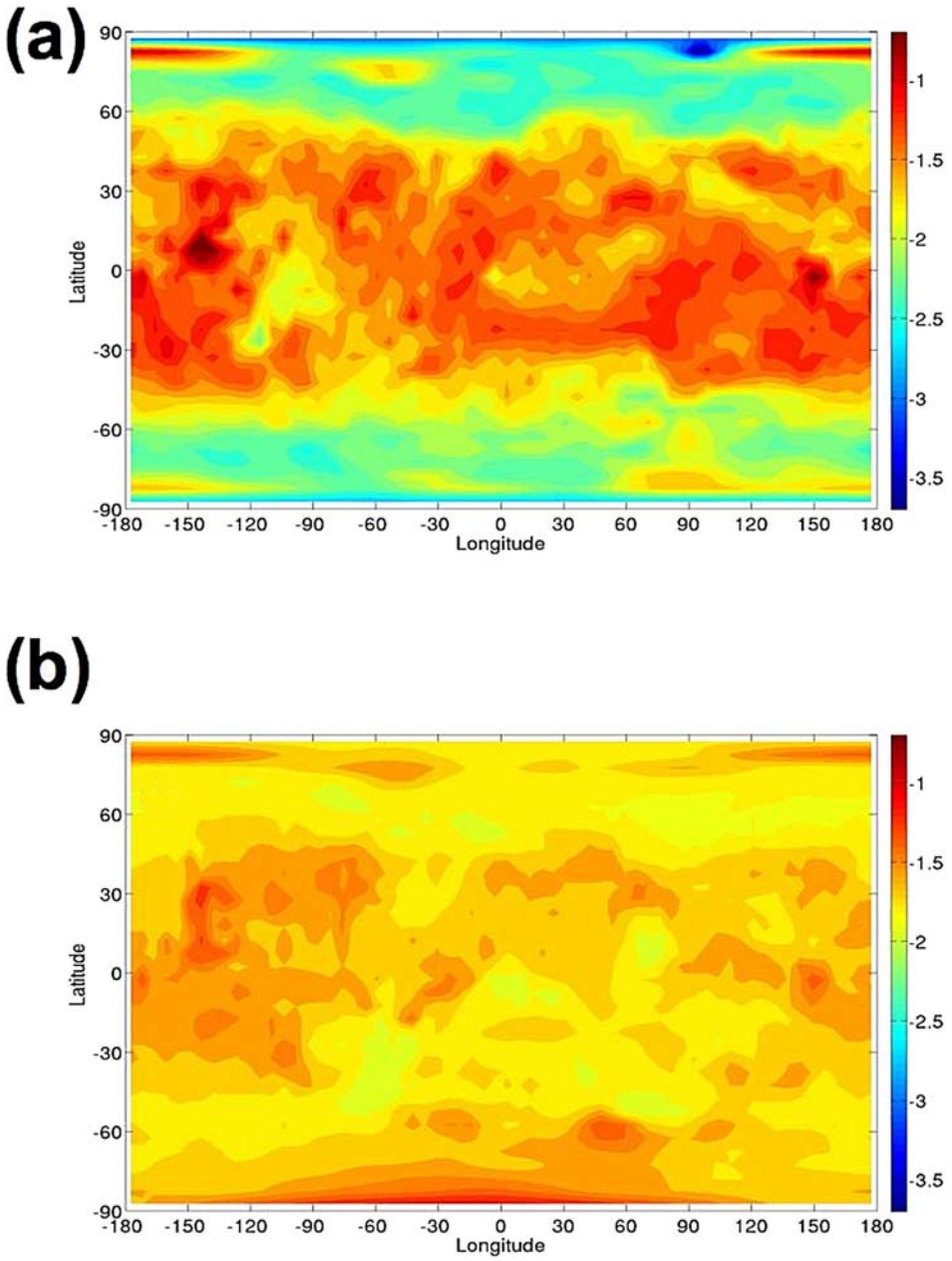

Figure 4. (a) The $\log_{10}$ (z_0) (m) inferred from C(10 m) interpolated to the standard 36 × 64 Mars implementation of the Planetary Weather Research and Forecasting Model (MarsWRF) grid and (b) $\log_{10}$ (z_0) (m) inferred from Mars Observer Laser Altimeter (MOLA) optical pulse width RMS slope-corrected roughness interpolated to the standard 5° × 5.625° (36 × 64) MarsWRF grid. The color stretch is identical for Figures 4a and 4b.

al. [2007]. The simulations use a prescribed atmospheric dust distribution that varies with time and location to determine dust radiative heating. Its form is chosen to closely reproduce the atmospheric temperatures observed by Mars Global Surveyor instruments during Mars year (MY) 24 (a year without major dust storms) and was developed by the Laboratoire de Météorologie Dynamique–University of Oxford Atmospheric, Oceanic, and Planetary Physics modeling partnership [*Forget et al.*, 1999] for use in producing simulations for their Mars climate database [*Lewis et al.*, 1999]. Interannual variability in the model is therefore limited. All data presented here are from year 8 of the simulations. Model data were output every 3 model hours.

4.2. Boundary Layer Temperatures

[18] We first assess zonally averaged daytime temperatures throughout the year at 370 Pa (0.5 scale heights above the pressure datum of 610 Pa or ∼5000–6000 m above this datum) for comparison with the results of *Smith* [2004] (Figure 5a). Daytime temperatures at 370 Pa were derived by interpolating the potential temperature profile using pressure, using the interpolated potential temperature

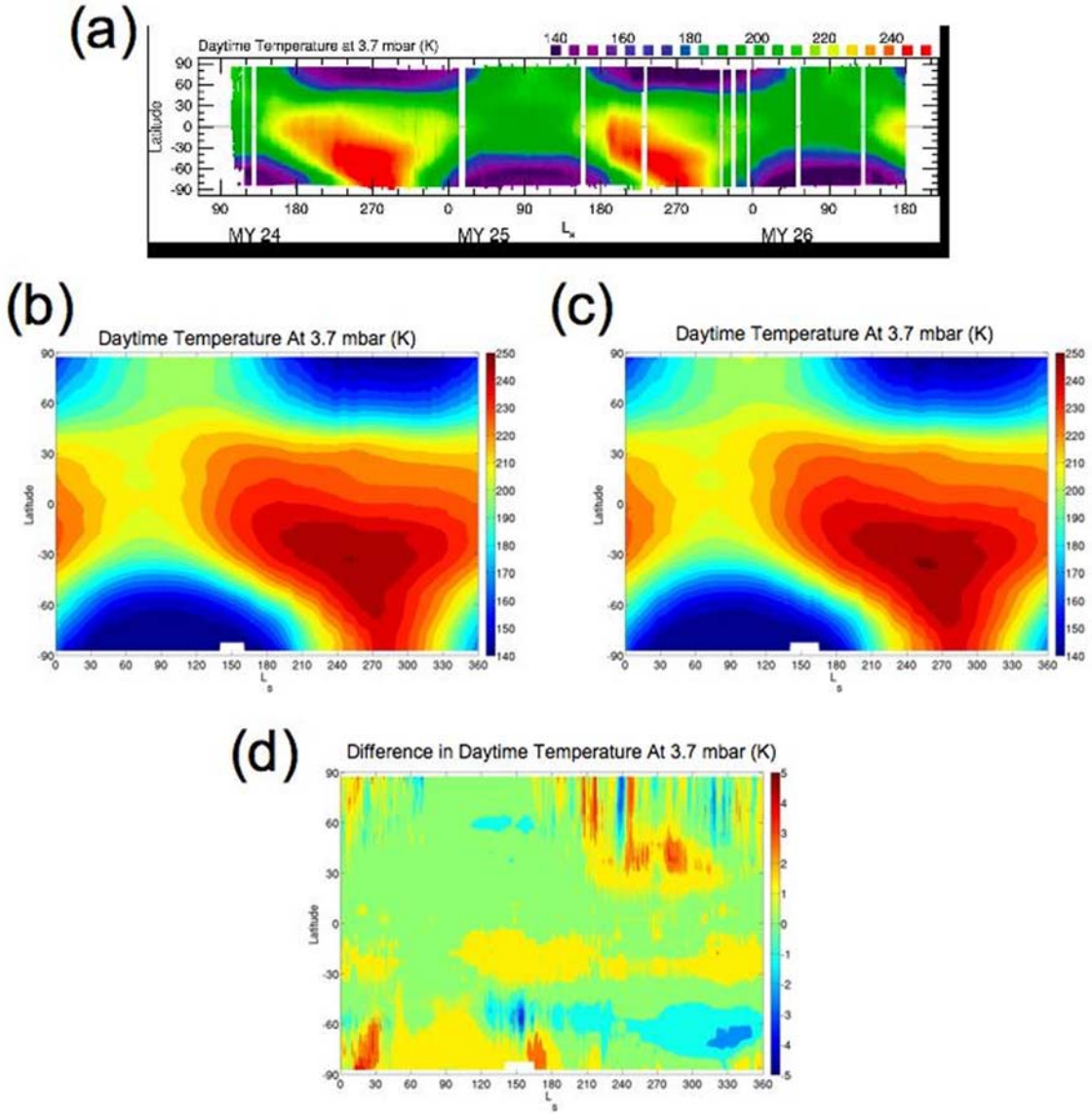

Figure 5. Zonally averaged daytime temperatures (K) at 370 Pa as a function of areocentric longitude (L_s). (a) Mars Global Surveyor Thermal Emission Spectrometer observations [*Smith*, 2004]. (b) MarsWRF simulation with topographically derived aerodynamic roughness map. (c) MarsWRF simulation with aerodynamic roughness map derived from MOLA pulse width total vertical roughness. (d) Difference between Figures 5b and 5c.

at 370 Pa to calculate the temperature at 370 Pa, and then taking the maximum temperature during each sol (Martian day) as the daytime temperature. In some cases the pressure at the surface was less than 370 Pa. In those cases the daytime 370 Pa temperature was not calculated, and these points were excluded from averaging. The number of points excluded along each latitude band is normally less than 10, except for a brief period over the southern pole during the winter, which appears in white in Figures 5b–5d. This analysis is not an exact comparison to the data of *Smith* [2004], which were collected at approximately 1400 local solar time, not necessarily at the diurnal maximum in data output every 3 h. We are interested, however, in the differences between the simulations in the context of a possible observational constraint such as Thermal Emission Spectrometer 3.7 mbar temperatures, not in which simulation agrees most closely with Smith's results, which, after all, depend on more parameters than z_0.

[19] Figures 5b and 5c show the zonally averaged 370 Pa temperatures predicted by each simulation. The results of both simulations look quite similar to the results of *Smith* [2004], especially those in MY 24, which should produce little surprise since the prescribed dust forcing was designed to match temperatures observed during that year. Figure 5d shows the difference between Figures 5b and 5c. Particularly notable are warmer winter and colder summer temperatures (at least in the southern hemisphere) in the high latitudes in the simulation with topographically derived

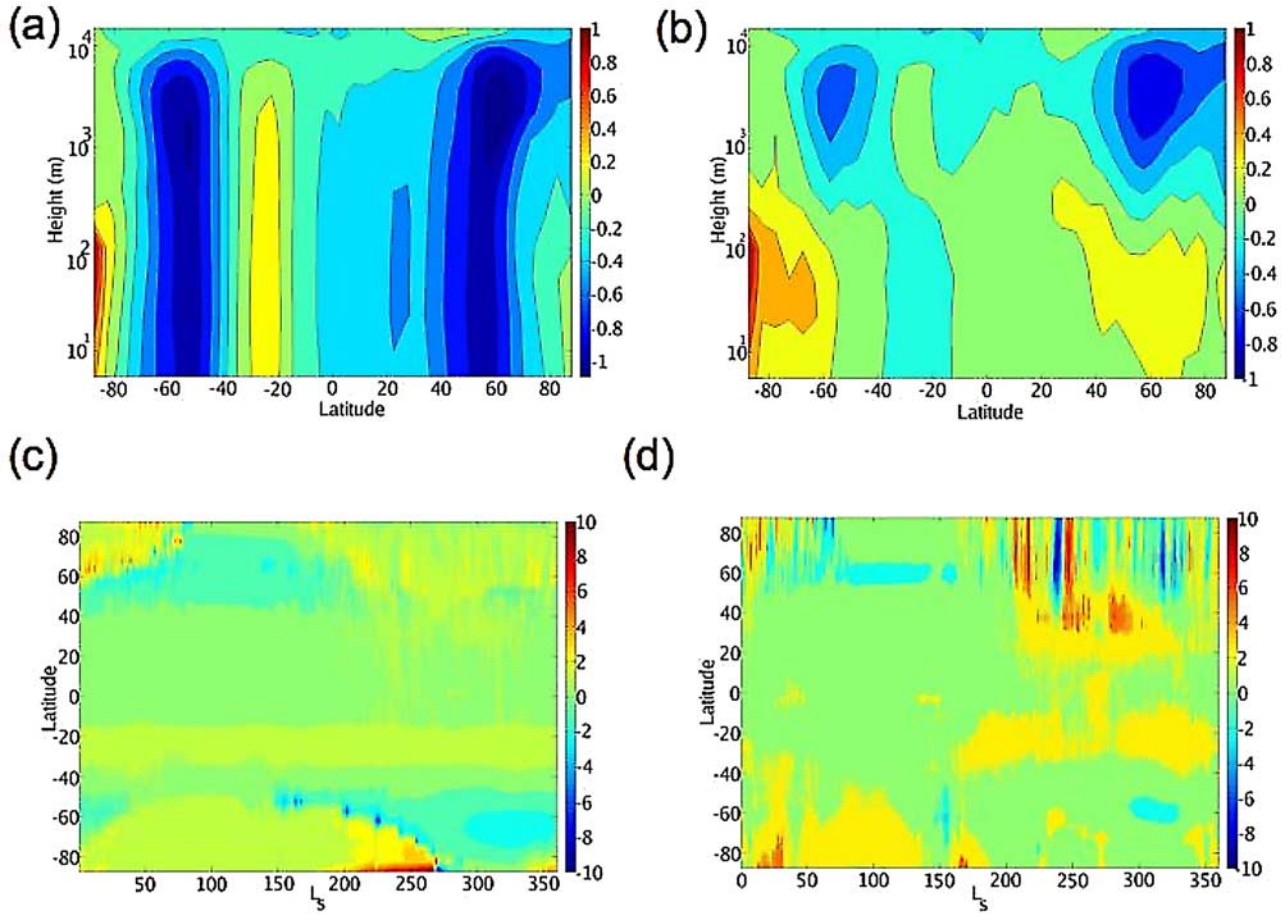

Figure 6. Plots of the differences between topographically derived roughness and pulse width roughness MarsWRF simulations. (a) Zonally averaged annual mean daytime temperatures as a function of approximate height above the surface (K). (b) Zonally averaged annual mean nighttime temperatures as a function of approximate height above the surface (K). (c) Zonally averaged daytime temperatures as a function of L_s (K) at an approximate height of 50 m. (d) Zonally averaged daytime temperatures as a function of L_s (K) at an approximate height of 9000 m.

roughness. Note also the narrow oscillatory features in the difference map during northern winter, which are simply due to differences between the timing of atmospheric waves in the two simulations.

[20] Because the boundary layer is the locus of surface influence on the atmosphere, the sensitivity of boundary layer temperatures to z_0 should be easiest to see by comparing temperatures at the same height above the surface rather than the same pressure level. Because of the large seasonal pressure variations on Mars an isobaric temperature plot will capture different parts of the boundary layer during different seasons. The model levels, however, have constant $P_{\text{level}}/P_{\text{sfc}}$, where P_{sfc} is the surface pressure, so each model level is fairly similar in height above the surface; for example, model level 3 ranges from 49 to 54 m above the surface, and model level 12 ranges from 8720 to 9530 m above the surface in northern spring. The sensitivity of the model level heights to pressure might result in artifacts because of differences in the pressure cycle between the models, but as we will discuss in section 4.3, pressure variations between the two simulations are minor; thus the model level height above the surface in one simulation at a particular point in time and space should be very similar to the corresponding point in the other simulation. Figures 6a and 6b show the differences in the simulations between zonally averaged daytime and nighttime temperatures, respectively. These differences are small (up to 1 K), but the major differences correspond quite closely to the high-latitude regions that are smoother in the topographically derived map. The low-latitude warming corresponds to a region that is clearly rougher in the topographically derived map. Most of the temperature differences appear in the daytime, with the exception of the polar differences.

[21] Figures 6c and 6d show seasonal variability in zonally averaged temperatures at ~50 m and ~9 km, marking the lower and upper ends of the boundary layer over most of the planet. The analogous difference plots at intermediate heights within the boundary layer look much like Figure 6c, showing slightly warmer temperatures (up to 1 K) in the topographically derived roughness simulations in the low latitudes of the southern hemisphere throughout much of the year, cooler temperatures in the high latitudes during the summer (up to 3 K), and warmer temperatures at

the south pole during spring deglaciation (up to 10 K). By model level 12 these features are difficult to see, and at higher levels the only differences in temperatures are due to shifts between the simulations in the timing of atmospheric waves, as observed in northern winter at the high latitudes in Figure 6d.

[22] The atmospheric wave features in northern winter accentuate the similarities between Figures 5d and 6d. Their major difference is that Figure 5d shows cooler temperatures in the southern hemisphere high latitudes in the topographically derived roughness map simulation not seen in Figure 6d. These particular features of Figure 5d suggest that our concerns about isobaric analyses were entirely justified. The 370 Pa level should be roughly 5000–6000 m above a surface with mean pressure of 610 Pa. However, Figure 5d looks like a mixture between a constant height plot at 9000 m above the surface and a constant height plot deeper within the boundary layer. Much of the Martian surface (with the exception of the southern highlands), however, is well below the 610 Pa datum in altitude. Thus the 370 Pa pressure level is well within the boundary layer during southern summer but not within it in northern summer.

[23] Therefore the differences in high-latitude summer temperatures between the simulations are quite real and suggest that heat transport by turbulent eddies dominates convective heat transport because temperatures are cooler over smoother terrain. To demonstrate this, we refer directly to the medium-range forecast model boundary layer scheme used by MarsWRF, in which vertical heat diffusion is governed by a surface similarity function, ϕ_t [*Hong and Pan*, 1996; *Sorbjan*, 1989]. Perhaps the most intuitive way to understand ϕ_t is as an inverse nondimensionalized vertical heat diffusivity, which is implied by Hong and Pan's definition of the Prandtl number as a function of ϕ_t/ϕ_m, where ϕ_m is the surface similarity function of vertical momentum transport. Thus efficient heat transport corresponds to small ϕ_t, and inefficient heat transport corresponds to large ϕ_t.

[24] In neutral and unstable conditions, $\phi_t = (1 - 1.6\eta/\Lambda)^{-1/2}$, and in stable conditions, $\phi_t = (1 + 0.5\eta/\Lambda)$, where Λ is the Obukhov length and η is the boundary layer height, which is not an independent parameter (and thus is sensitive to z_0) but is computed iteratively within the boundary layer scheme in order to yield an idealized diffusivity profile. Λ is strongly dependent on z_0 through its cubic dependence on u^* (see the discussion of (7) in section 4.4). Thus smooth areas generally will have a low magnitude of Λ and vice versa. Note that Λ is negative when surface heat flux is positive and vice versa. So if heat transport due to free convection dominated in the MarsWRF simulations, the rate of vertical heat transport would be proportionate to $\phi_t^{-1} \sim (-\eta/\Lambda)^{1/2}$ or $\Lambda^{-1/2}$. Thus smoother terrains under unstable conditions (Λ negative and small in magnitude) should have strong heat transport from the surface and warmer boundary layer temperatures.

[25] To make this last approximation, we have used the fact that $\eta \gg -\Lambda$ in free convective boundary layers. Within the boundary layer scheme this fact arises from a dependence of η on the inverse of the difference between the virtual potential temperature at the top of the boundary layer and the potential temperature just above the surface, $(\theta_v\eta - \theta_s)^{-1}$, and the structure of a free convective boundary layer. Such a boundary layer is divided into three parts: (1) a thin surface unstable layer, where θ decreases with height; (2) a much thicker mixed layer, where θ is roughly constant with height; and (3) an inversion layer, where θ increases with height and radiative heat fluxes dominate. Ideally, η should be diagnosed at a level of neutral buoyancy at which the positive buoyancy imparted by the unstable layer matches the negative buoyancy imparted by the inversion layer. In the context of the iteration, if η is overestimated, $\theta_v \sim \theta$ is diagnosed deep within the inversion layer, where $\theta \gg \theta_s$, reducing the estimate of η. If η is underestimated, $\theta_v \sim \theta$ is diagnosed in the mixed layer, where $\theta \sim \theta_s$, greatly increasing the estimate of η. The sensitivity of η to z_0 enters through the unstable layer. If forced convective transport is relatively inefficient because of small z_0, the air near the surface will be strongly heated and positively buoyant and only will lose buoyancy by mixing with high θ air at altitude, resulting in large values of η under the same conditions in which the absolute magnitude of Λ tends to be small.

[26] In neutral and stable conditions the rate of vertical heat transport will be proportionate to $\phi_t^{-1} \sim (\eta/\Lambda)^{-1}$ or just Λ, for $|\eta/\Lambda| > 2$, so smoother terrains (Λ positive and small in magnitude) should have less heat transport from the surface and cooler boundary layer temperatures. Since the surface is warmer than the atmosphere at the high latitudes during the summer and smoothing the high latitudes during the summer results in cooling of the boundary layer, vertical heat transport apparently is weaker over smoother terrain in this case. Thus we may infer that mechanical (forced convective) heat transport dominates over (free) convective heat transport.

[27] Moreover, the dominance of mechanical heat transport is also suggested by the warmer temperatures observed throughout the year in the low latitudes of the southern hemisphere since strong insolation is persistent there. In the topographically derived roughness map these latitudes are rougher, so a relative warming implies that mechanical heat transport (whose efficiency increases with roughness) is dominant over convective heat transport (whose efficiency decreases with roughness). Note that this analysis only demonstrates the dominant heat transport process in MarsWRF, not necessarily the dominant heat transport process on Mars.

[28] Of higher magnitude are the warmer temperatures over the south pole during sublimation in southern spring (L_s = 210°–260°). A similar but weaker feature is seen during northern hemisphere spring, suggesting some connection with the smoothness of the polar regions in the topographically derived roughness map, especially the much smoother south pole. Here too weaker mechanical heat transport is having an effect, but the temperature gradient is the opposite of that in the high latitudes in summer and the tropics throughout the year. Here temperature increases with height because a very cool sublimating surface underlies an atmosphere being warmed by the late spring Sun. Weaker mechanical heat transport over the relatively smoother terrain limits mixing of the boundary layer with cool near-surface air, resulting in warmer boundary layer temperatures.

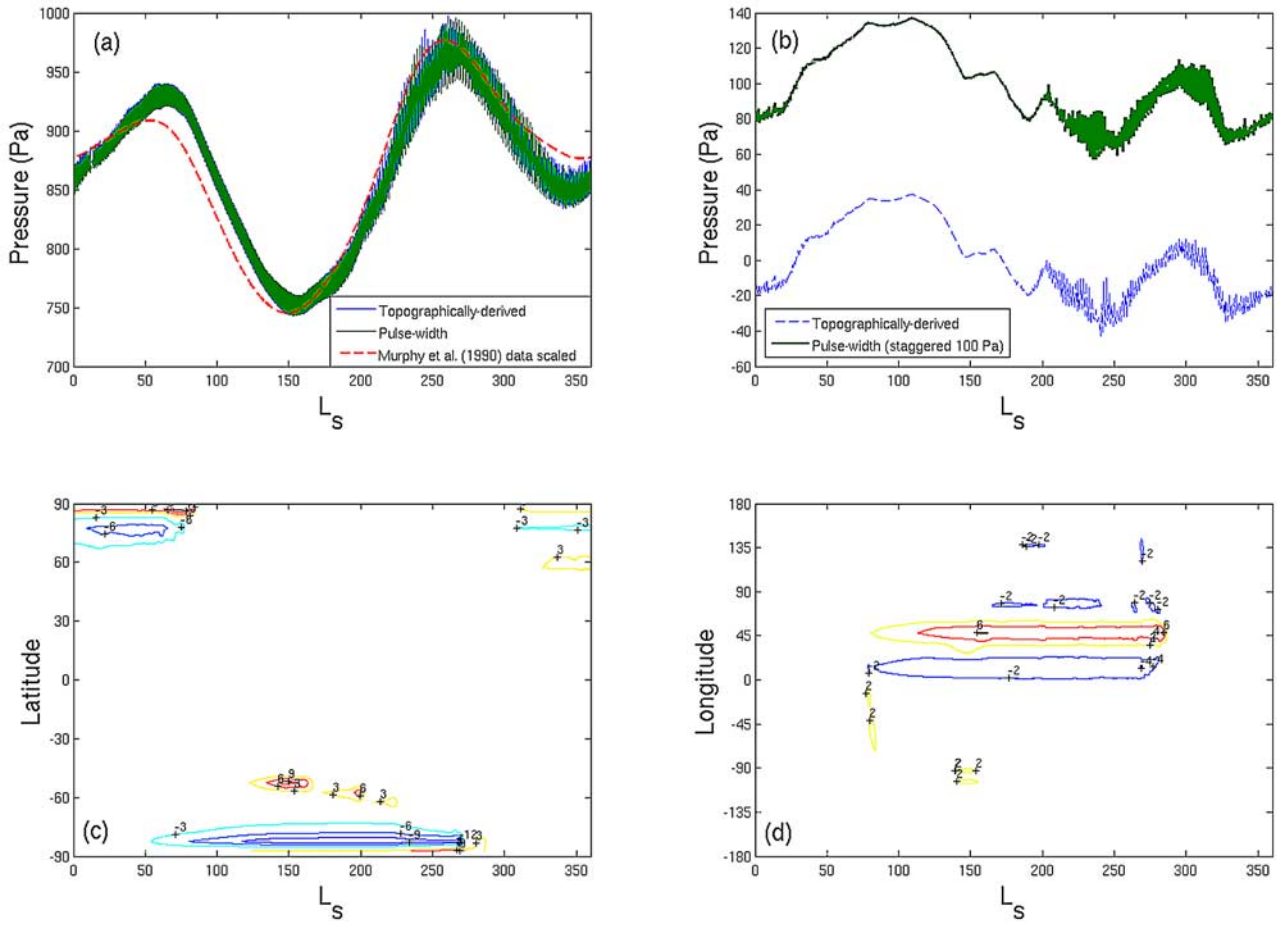

Figure 7. (a) Viking Lander 1 (VL1) pressure cycle in the MarsWRF simulations using topographically derived roughness, pulse width roughness, and *Murphy et al.*'s [1990] smoothed version of VL1 pressure cycle observations adjusted to the atmospheric mass of the MarsWRF simulations (dashed line). (b) Difference between the VL1 pressure cycles in the MarsWRF simulations and *Murphy et al.*'s [1990] smoothed version of VL1 pressure cycle observations adjusted to the atmospheric mass of the MarsWRF simulations. The pulse width roughness simulation results are staggered by 100 Pa for clarity. (c) Zonally averaged CO_2 ice surface density as a function of L_s (kg m^{-3}). Typical ice surface densities are ~300–1000 kg m^{-2}. (d) Meridionally averaged CO_2 ice surface density as a function of L_s (kg m^{-3}).

4.3. Pressure Cycle and Related Processes

[29] The sensitivity of late spring polar temperatures to z_0 discussed in section 4.2 suggests an interesting question. What effect does z_0 or the relative magnitude of turbulent eddy transport have on the pressure cycle? This is not an esoteric question. In Figure 7a we show the pressure predicted by interpolation of model output to the Viking Lander 1 (VL1) site by each MarsWRF simulation in comparison with a smoothed version of the VL1 pressure sensor data [*Murphy et al.*, 1990]. These data have been scaled to correct for a ~10% discrepancy between the atmospheric mass in the model and the total atmospheric mass of Mars. Note the difference in the phase of the cycle in the observations relative to the predictions of the simulations. This is a well-known issue in Mars GCMs generally [e.g., *Hourdin et al.*, 1993]. It should be clear from Figure 7a that roughness is not the magical lever on the phase of the pressure cycle, but in Figure 7b we show the difference between the VL1 pressure cycles predicted by these two MarsWRF simulations in comparison with the difference between the pulse width roughness simulation VL1 pressure cycle and the Murphy et al. VL1 data corrected for atmospheric mass assumptions as before. Clearly, z_0 has little effect on the phase discrepancy. The seasonal variation in the amplitude in the first difference curve seems due to differences between the simulations in the timing of atmospheric waves. Figures 7c and 7d show differences between the simulations in zonally and meridionally averaged CO_2 ice cover. Despite the large sensitivity in temperatures to changes in z_0, these temperature differences make very little difference in ice cover (~2% at most). Changing the magnitude of eddy diffusion only changes how heat is redistributed. It cannot add more heat to the system. Thus the roughness of the poles and high latitudes has little direct effect on the pressure cycle.

[30] There is one effect of sublimation and condensation we have neglected in this study. We have not considered how z_0 might change with the deposition and removal of

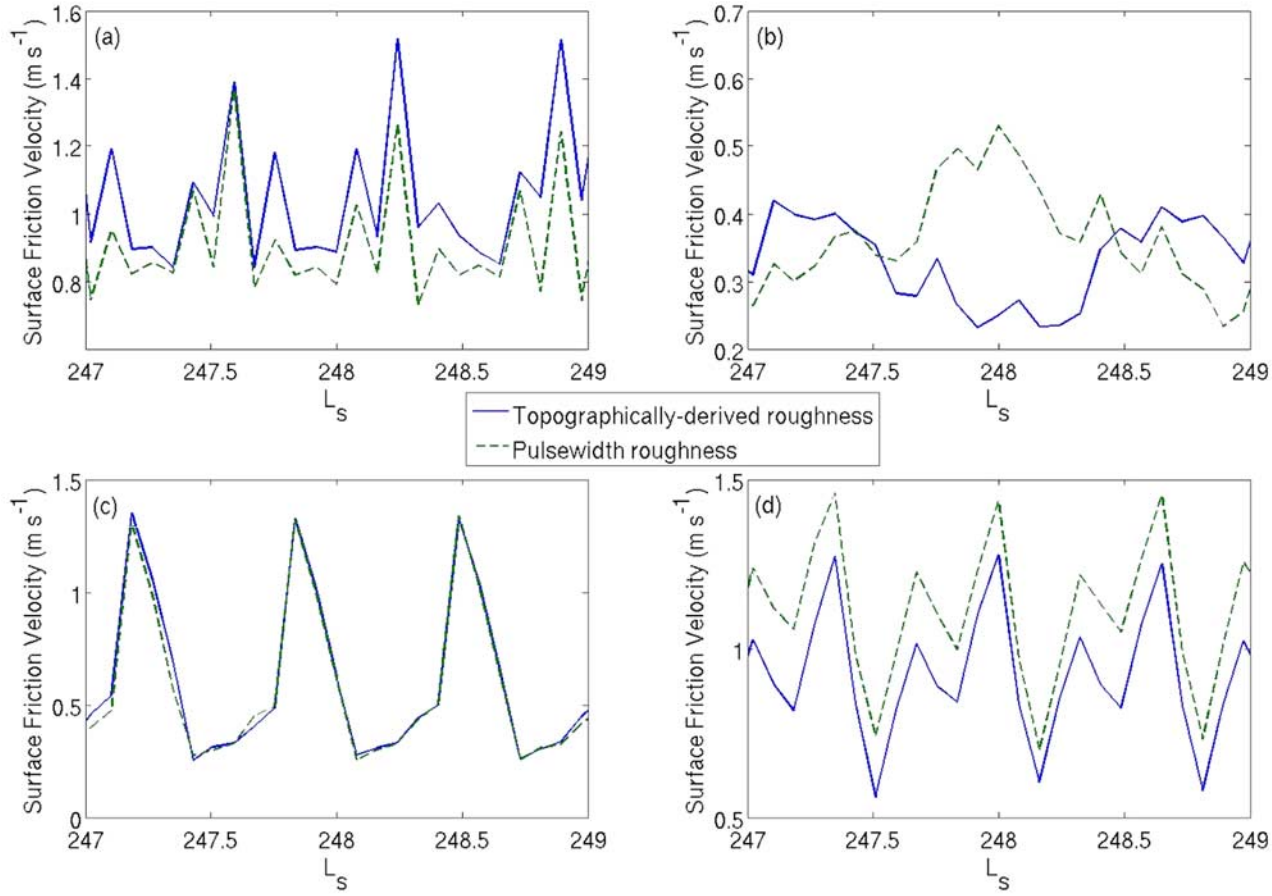

Figure 8. Comparison of surface friction velocity (m s^{-1}) output at various locations on Mars for the simulations using the topographically derived and pulse width roughness maps from L_s = 247°–249°: (a) 12.5°N, −143.4375°E ($z_{0,\text{topographically derived}}$ = 0.1189 m; $z_{0,\text{pulse width}}$ = 0.0594 m); (b) 82.5°N, 92.8125°E ($z_{0,\text{topographically derived}} = 2 \times 10^{-4}$ m; $z_{0,\text{pulse width}}$ = 0.02 m); (c) 2.5°S, −8.4375°E ($z_{0,\text{topographically derived}}$ = 0.0174 m; $z_{0,\text{pulse width}}$ = 0.0175 m); and (d) 62.5°S, 64.6875°E ($z_{0,\text{topographically derived}} = 3.4 \times 10^{-3}$ m; $z_{0,\text{pulse width}}$ = 0.0287 m).

CO_2 ice. The change in surface roughness is dependent on the microphysics of the ice deposition and sublimation processes and thus is a problem in solid state physics rather than atmospheric science. While understanding these changes is not critical for understanding global dynamics, it may be important for understanding polar boundary layer dynamics. However, the particular relation between ice deposition microphysics and surface roughness is beyond the scope of atmospheric modeling, and its definition will require detailed laboratory experiments.

4.4. Limitations of Prescribed Dust Forcing

[31] Taken as a whole, the boundary layer temperature sensitivity of MarsWRF to plausible Martian roughness conditions may be important locally but appears to be irrelevant to the simulation of global dynamics. However, these simulations use a specified prescribed dust forcing and thereby neglect a potential z_0-related feedback. The aerodynamic roughness height is used to determine u^*, a critical input to any dust-lifting parameterization. Figure 8 shows some example plots of u^* that can illustrate the importance of the sensitivity of dust lifting to z_0 through u^*. To first order these plots can be explained in terms of the "logarithmic layer" model of boundary layer wind speed mentioned in section 1. If the wind speed at a height of z has the same value, $U(z)$, in both of the simulations, then

$$\frac{u^*_{\text{pulse width}}}{u^*_{\text{topographically derived}}} = \frac{\ln \frac{z}{z_{0,\text{topographically derived}}}}{\ln \frac{z}{z_{0,\text{ pulse width}}}}. \tag{7}$$

The right-hand side of (7) is a constant for a particular location, so in this simplification the friction velocity traces should be identical in shape and should differ in magnitude by a constant factor. This is very nearly true in Figures 8a, 8c, and 8d but is not obvious in Figure 8b, where differences in the timing of wave activity between the two simulations (as seen in Figures 5d and 6d) result in different wind speeds at z (10 m in the model). Differences between the traces to higher order in the other plots are due to either timing of wave activity or very limited feedback between the roughness parameter and the circulation. However, these constant factor differences in u^* still can produce a very nonlinear effect on dust transport. For instance, in Figure 8a the simulation using the topographically derived roughness

map outputs $u^* = \sim 1.5$ m s^{-1} at the same time that the simulation using the pulse width roughness map outputs $u^* = \sim 1.2$ m s^{-1}. *Greeley and Iversen* [1985] note that the minimum threshold surface friction velocity varies between 1 and 2 m s^{-1} for Mars conditions. Thus, depending on the assumptions of the dust transport model used, a simulation using the topographically derived roughness map might diagnose active saltation resulting in dust transport, whereas a simulation using the other map might have no dust transport at all. Also, since saltation dust fluxes typically have a quadratic to quartic dependence on the difference between the surface friction velocity and the threshold friction velocity [*Shao*, 2000], small differences in surface friction velocity might not just mean the difference between no dust transport and a little dust transport but between a little dust transport and a great deal of dust transport.

[32] The dependence of dust transport on z_0 might produce much greater temperature sensitivity to z_0 than is demonstrated in this study. The difference in mean boundary layer temperatures between a clear ($\tau = 0$) and dusty atmosphere ($\tau = 1$) can be $\sim$8 K, and the differences in the average daytime and nighttime temperatures can be greater [*Pollack et al.*, 1990]. Preliminary MarsWRF simulations, considering only dust lifting by convective vortices (dust devils), have produced 5–7 K differences in boundary layer temperatures because of an *e*-fold change in z_0 (C. E. Newman, personal communication, 2007). The effects on the model's global dynamics due to changes in initiation of dust storm lifting may be even more important. Thus this study will serve as a useful baseline for future experiments on the sensitivity of dust-lifting processes and the atmosphere in general to plausible roughness conditions. We plan such work in the near future as part of a concerted effort to improve the parameterization of dust-lifting processes in GCMs for both terrestrial and Martian applications.

5. Summary

[33] We have investigated the sensitivity of the Martian boundary layer in a GCM to the aerodynamic roughness parameter (z_0). Rather than investigate the sensitivity using idealized maps of z_0, we chose to use various MOLA data sets to develop two high-resolution maps of z_0. Because of the limited amount of calibration data and some methodological uncertainties we do not claim that either map is an accurate representation of z_0 for Mars, only that they span a plausible range of z_0 on Mars at a particular point. We then used each map to force the boundary layer parameterizations in MarsWRF and examined the differences between boundary layer temperatures and the pressure cycle simulated using each map of z_0. The major differences between the simulations were due to the effect of z_0 on the intensity of vertical heat transport within the boundary layer by forced convection during the daytime. Higher z_0 enhanced forced convective (mechanical) heat transport and vice versa. Differences in daytime boundary layer temperatures due to this effect were as great as 10 K seasonally (at the south pole) but were generally much less. Perturbations to the pressure cycle due to changes in vertical heat transport at the poles were minimal. These simulations, however, used a prescribed dust forcing, and thus only provide a minimum estimate for the sensitivity of boundary layer temperatures to the assumed aerodynamic roughness parameter.

Notation

- α roughness constant of scale invariance, m.
- c curvature of topography, m^{-1}.
- C interquartile width of the curvature of topography, m^{-1}.
- ϕ_m surface similarity function of vertical momentum transport.
- ϕ_t surface similarity function of vertical heat transport.
- F fractional occupation by roughness elements.
- η boundary layer height, m.
- h roughness elemental or topographic height, m.
- H Hurst exponent (Hausdorff measure).
- Λ Obukhov length, m.
- L horizontal baseline, m.
- μ_n *n*th statistical moment.
- n degree of sensitivity of the aerodynamic roughness element to the standard deviation of topographic height.
- N_o number of sites occupied by roughness elements.
- N_s number of sites.
- σ_h standard deviation of topographic height.
- θ potential temperature, K.
- U wind speed, m s^{-1}.
- u^* surface friction velocity, m s^{-1}.
- z height above surface, m.
- z_0 aerodynamic roughness parameter, m.

[34] **Acknowledgments.** This manuscript has benefited greatly from input by C. E. Newman, A. Soto, C. Lee, and an anonymous reviewer. This work was supported by the National Aeronautics and Space Administration through the Mars Data Analysis Program and the Applied Information Systems Research Program.

References

Chen, F., Z. Janjic, and K. Mitchell (1997), Impact of atmospheric surface-layer parameterizations in the new land-surface scheme of the NCEP mesoscale Eta model, *Boundary Layer Meteorol.*, *85*, 391–421.

Dong, Z., X. Lu, and X. Wang (2002), Aerodynamic roughness of gravel surfaces, *Geomorphology*, *43*, 17–31.

Forget, F., F. Hourdin, R. Fournier, C. Hourdin, O. Talagrand, M. Collins, S. R. Lewis, P. L. Read, and J.-P. Huot (1999), Improved general circulation model of the Martian atmosphere from the surface to above 80 km, *J. Geophys. Res.*, *104*, 24,155–24,176.

Garvin, J. B., J. J. Frawley, and J. B. Abshire (1999), Vertical roughness of Mars from the Mars Orbital Laser Altimeter, *Geophys. Res. Lett.*, *26*, 381–384.

Greeley, R., and J. D. Iversen (1985), *Wind as a Geological Process: On Earth, Venus, and Titan*, Cambridge Univ. Press, Cambridge, U. K.

Greeley, R., D. G. Blumberg, J. F. McHone, A. Dobrovolskis, J. D. Iversen, N. Lancaster, K. R. Rasmussen, S. D. Wall, and B. R. White (1997), Applications of spaceborne radar laboratory data to the study of aeolian processes, *J. Geophys. Res.*, *102*, 10,971–10,983.

Greeley, R., et al. (2006), Active dust devils in Gusev crater, Mars: Observations from the Mars xploration Rover Spirit, *J. Geophys. Res.*, *111*, E12S09, doi:10.1029/2006JE002743.

Hébrard, E., P. Coll, F. Montmessin, B. Marticorena, and G. Bergametti (2007), Modelling the aeolian erosion thresholds on Mars, paper presented at 7th International Conference on Mars, Mars Explor. Program, Pasadena, Calif., 9–13 Jul.

Hong, S.-Y., and H.-L. Pan (1996), Nonlocal boundary layer vertical diffusion in a medium-range forecast model, *Mon. Weather Rev.*, *124*(10), 2322–2339.

Hourdin, F., P. Levan, F. Forget, and O. Talagrand (1993), Meteorological variability and the annual surface pressure cycle on Mars, *J. Atmos. Sci.*, *50*, 3625–3640.

Kreslavsky, M. A., and J. W. Head (2000), Kilometer-scale roughness of Mars: Results from MOLA data analysis, *J. Geophys. Res.*, *105*, 26,695–26,711.

Lewis, S. R., M. Collins, P. L. Read, F. Forget, F. Hourdin, R. Fournier, C. Hourdin, O. Talagrand, and J. P. Huot (1999), A climate database for Mars, *J. Geophys. Res.*, *104*, 24,177–24,194.

Marticorena, B., et al. (2006), Surface and aerodynamic roughness in arid and semiarid areas and their relation to radar backscatter coefficient, *J. Geophys. Res.*, *111*, F03017, doi:10.1029/2006JF000462.

Menenti, M., and J. C. Ritchie (1992), Estimation of effective aerodynamic roughness with altimeter measurements, paper presented at International Geoscience and Remote Sensing Symposium, Inst. of Electr. and Electron. Eng., Houston, Tex., 26–29 May.

Murphy, J. R., C. B. Leovy, and J. E. Tillman (1990), Observations of the Martian surface winds at the Viking Lander 1 site, *J. Geophys. Res.*, *95*, 14,555–14,576.

Neumann, G. A., J. B. Abshire, O. Aharonson, J. B. Garvin, X. Sun, and M. T. Zuber (2003), Mars Orbiter Laser Altimeter pulse width measurements and footprint-scale roughness, *Geophys. Res. Lett.*, *30*(11), 1561, doi:10.1029/2003GL017048.

Obukhov, A. M. (1946), Turbulentnost' v temperaturnoj-neodnorodnoj atmosphere, *Tr. Inst. Teor. Geofiz. Akad. Nauk SSSR*, *1*, 95–115.

Papoulis, A. (1991), *Probability, Random Variables, and Stochastic Processes*, 3rd ed., McGraw-Hill, New York.

Pollack, J. B., R. M. Haberle, J. Schaeffer, and H. Lee (1990), Simulations of the general circulation of the Martian atmosphere: 1. Polar processes, *J. Geophys. Res.*, *95*, 1447–1473.

Prigent, C., I. Tegen, F. Aires, B. Marticorena, and M. Zribi (2005), Estimation of the aerodynamic roughness length in arid and semi-arid regions over the globe with the ERS scatterometer, *J. Geophys. Res.*, *110*, D09205, doi:10.1029/2004JD005370.

Richardson, M. I., A. D. Toigo, and C. E. Newman (2007), PlanetWRF: A general purpose, local to global numerical model for planetary atmospheric and climate dynamics, *J. Geophys. Res.*, *112*, E09001, doi:10.1029/2006JE002825.

Shao, Y. (2000), *Physics and Modelling of Wind Erosion*, Kluwer Acad., Dordrecht, Netherlands.

Shepard, M. K., B. A. Campbell (1998), Fractal planets: A generalized surface roughness model for remote sensing, *Proc. Lunar Planet. Sci. Conf.*, 29th, abstract 1235.

Smith, M. D. (2004), Interannual variability in TES atmospheric observations during 1999–2003, *Icarus*, *167*, 148–165.

Sorbjan, Z. (1989), *Structure of the Atmospheric Boundary Layer*, Prentice-Hall, Englewood Cliffs, N. J.

Sullivan, R. (2002), Threshold-of-motion wind friction speeds at the Mars Pathfinder landing site, *Proc. Lunar Planet Sci. Conf.*, *33rd*, abstract 2002.

Sullivan, R., R. Greeley, M. Kraft, G. Wilson, M. Golombek, K. Herkenhoff, J. Murphy, and P. Smith (2000), Results of the Imager for Mars Pathfinder windsock experiment, *J. Geophys. Res.*, *105*, 24,547–24,562.

Sullivan, R., et al. (2005), Aeolian processes at the Mars Exploration Rover Meridiani Planum landing site, *Nature*, *436*, 58–61, doi:10.1038/nature03641.

Turcotte, D. L. (1992), *Fractals and Chaos in Geology and Geophysics*, Cambridge Univ. Press, New York.

Wilson, R. J., and K. Hamilton (1996), Comprehensive model simulation of thermal tides in the Martian atmosphere, *J. Atmos. Sci.*, *53*(9), 1290–1326.

N. G. Heavens and M. I. Richardson, Division of the Geological and Planetary Sciences, California Institute of Technology, MC 150-21, 1200 E. California Boulevard, Pasadena, CA 91125, USA. (heavens@gps.caltech.edu)

A. D. Toigo, Center for Radiophysics and Space Research, Cornell University, Ithaca, NY 14853, USA.